On-Chip Positionable Waveguides for Submicrometric Photonic Alignment

Tjitte-Jelte Peters and Marcel Tichem

***Abstract*— In this paper, we present positionable photonic waveguide arrays that are developed for optical chip-to-chip alignment. Partly suspended photonic structures, based on the Si_3N_4/SiO_2 material platform, are equipped with thermal actuators enabling the free end of the structures to be positioned with submicrometer accuracy. A finite-element model is developed to provide insight in the way the design of the system affects the performance. The modeling results show that the expected vertical deflection and rotation are highly dependent on the array design. Measurements of fabricated devices confirm the trends that follow from the model and are used to assess the positioning performance. Moreover, the finite-element analysis gives guidelines for the design parameters of an optimal positionable photonic waveguide array. By following these guidelines, all the requirements for the intended photonic alignment can be fulfilled, which is validated by measurements. The stability over time of the positioning system is experimentally determined and is also sufficient. Measured mode field profiles of partly suspended waveguide beams with 1 μm × 220 nm (width × thickness) sized waveguide cores show correct waveguiding functionality. Finally, an alignment experiment demonstrates how three adjacent waveguide beams within a positionable waveguide array can be actively aligned with the channels of another photonic chip. [2017-0046]**

***Index Terms*— Microactuators, microelectromechanical devices, photonic waveguide, flexible structures, photonic alignment, submicrometric alignment.**

I. Introduction

PACKAGING, which is the integration of components in a housing, is a large contributor to the overall cost of photonic end products. Photonic integrated circuits (PICs) used to be the most expensive components of photonic packages. As the design and manufacturing technology of PICs have evolved over the past decades, fairly complex chips can now be produced against reasonable cost. However, the developments in packaging are lagging behind. As a result, particularly when multiple optical and electrical connections are required, the packaging costs become dominant.

Particularly the precision alignment of photonic components amounts to a substantial part of the packaging costs. Realizing electrical connections to a PIC benefits from the established field of microelectronics, whereas making optical connections is less straightforward because of the tight alignment tolerances required for low optical loss. Because of the variety in PIC material platforms and package configurations, the photonic alignment commonly relies on tailor-made solutions.

This lack of standardization hampers photonic applications to make the transition from a research state to a commercial product [1]–[3]. Automation of photonic alignment is challenging and the use of dedicated robotic assembly systems may lead to substantial cycle times. A cycle-time (including process setup time) in the order of one hour is mentioned in [4] for the active alignment of a single mode fiber with a grating coupler.

For the future of PICs, it is crucial that photonic alignment technology catches up with the developments of photonics in general. As integrated photonics technology matures, the number of optical ports grows, increasing the difficulty of photonic alignment even further.

A novel alignment concept [5], offering an increased level of automation, has the potential to replace the customized alignment solutions applied in many photonic applications. The essence of this alignment concept is to integrate mechanically flexible waveguides and positioning functions into a single PIC. This combination results in positionable waveguides that can be fine-aligned with the waveguides of another PIC. Once they are fine-aligned, the waveguides are to be locked in their optimal position for the lifetime of the product. This paper is limited to actuation in two directions: out-of-plane translation and rotation around the propagation direction of the light. For a fully functional system, also in-plane translation needs to be dealt with, as well as the position locking after alignment. Solutions for these functions are part of ongoing work and are not treated in this paper.

The research into integrating actuator technology and optical waveguides started more than two decades ago. In a review paper, Chollet distinguishes three types of co-integration: monolithic, hybrid and stacked co-integration [6]. The combinations mentioned in this review paper show a variety of waveguide materials, e.g. GaAs [7], InP [8], polymer [9], and Si [10]. The co-integration presented in the current paper falls in the stacked category, as thermal micro-electromechanical system (MEMS) actuators are integrated by depositing extra material on top of a silicon nitride (Si_3N_4)/silicon dioxide (SiO_2) waveguide material platform.

In this paper, we explore the design space of positionable photonic waveguide arrays (WGAs). The effect of relevant design parameters on post-release deformation and actuator performance is studied on the basis of a finite element model (FEM), and is substantiated by measurements

Manuscript received March 4, 2017; revised June 28, 2017; accepted July 16, 2017. Date of publication August 1, 2017; date of current version November 29, 2017. This work was supported by the STW Generic Technologies for Integrated Photonics Program under Grant 11355 (Flex-OGuides). Subject Editor S. Merlo. *(Corresponding author: Tjitte-Jelte Peters.)*

The authors are with the Precision and Microsystems Engineering, Delft University of Technology, CD Delft 2628, The Netherlands (e-mail: tjittejelte@gmail.com; m.tichem@tudelft.nl).

Color versions of one or more of the figures in this paper are available online at http://ieeexplore.ieee.org.

Digital Object Identifier 10.1109/JMEMS.2017.2729945

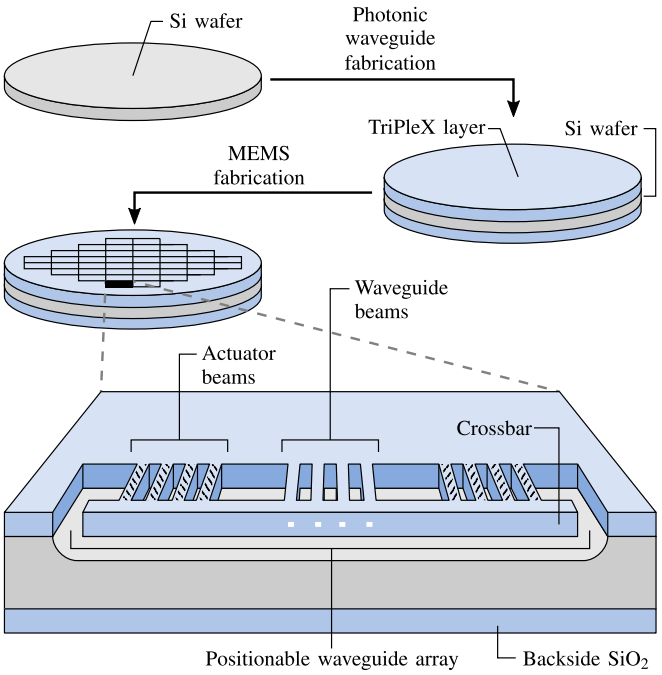

Fig. 1. Schematic overview of the fabrication of positionable WGAs. Top: the optical waveguide functionality is realized first, followed by the MEMS fabrication. Bottom: a close-up view of a single positionable WGA.

on realized WGAs. Design conditions for sub-micrometer precise alignment are established. In addition, we demonstrate, for the first time, optical chip-to-chip alignment using the proposed concept.

II. Design Parameters and Positioning Requirements

Positionable photonic waveguide arrays are developed and realized in photonic chips, based on a Si_3N_4/SiO_2 waveguide technology (TriPleX™ [11], proprietary to LioniX B.V., the Netherlands). The fabrication process consists of two consecutive sequences, as illustrated in Figure 1. First, photonic waveguides are created by the formation of a $SiO_2/Si_3N_4/SiO_2$ (lower cladding / core / upper cladding) layer stack on a silicon wafer. After that, the MEMS fabrication sequence creates mechanically flexible, suspended waveguide structures. The suspended waveguide structures consisting mostly of SiO_2 tend to fracture due to compressive residual stress in the SiO_2. A temporary reinforcement method is implemented to prevent the waveguide structures from fracturing at the moment they are released.

First, the photonic layer stack is plasma etched to obtain the desired waveguide structure pattern. The same pattern is then anisotropically etched into the underlying silicon. Next, an isotropic silicon etch releases the waveguide structures. By locally applying a passivation layer on the silicon sidewalls prior to this etch, the suspended waveguide structures are reinforced by a layer of silicon. This silicon reinforcement reduces the expansion and buckling, preventing the structure from fracturing. Electro-thermal actuators are integrated with the suspended structures by depositing and patterning poly-Si on top of the TriPleX material. More details on the fabrication process are published elsewhere [12].

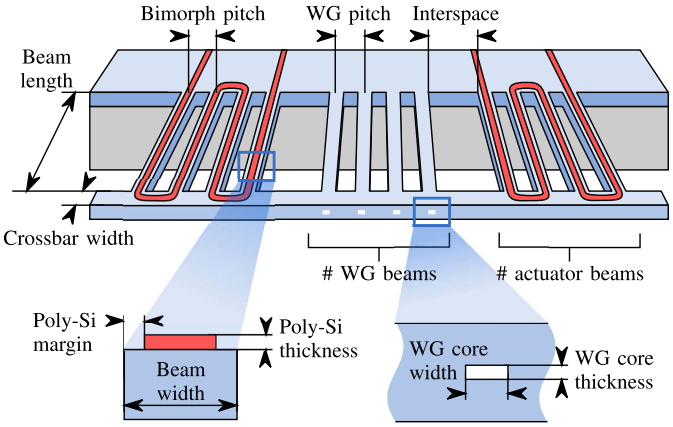

Fig. 2. Typical WGA layout, showing the design parameters of the system.

Positionable WGAs consist of waveguide beams and actuator beams that are designed with the same length and which are mechanically connected at their free ends by a crossbar, as illustrated in Figure 1. A number of waveguide beams, four in the figure, is situated at the center. A set of thermal actuator beams is placed on both sides of the waveguide beams, for out-of-plane motion and rotation around the propagation direction of the light.

The photonic waveguide beams are based on single stripe Si_3N_4 waveguide cores that are embedded in a SiO_2 cladding. These Si_3N_4 cores are 220 nm in thickness and up to 1.5 μm in width, ensuring they are mostly single-mode at a wavelength of 1550 nm. Moreover, 220 nm is a standard Si_3N_4 layer thickness for many applications that are based on the SiO_2/Si_3N_4 material platform. The waveguide beams have a total thickness of 16 μm and a total width of 18 μm. The actuator beams consist of SiO_2 beams (without waveguiding cores) with the same cross-sectional dimensions as the waveguide beams. To create thermal bimorph actuators, a strip of poly-Si is patterned on top of the beams. The poly-Si also functions as a resistive heater, the resistivity of which is determined by the level of boron doping applied.

The fabrication requires a total of six photolithography masks. A single 100 mm wafer comprises 140 chips, each measuring 6 mm $\times$ 6 mm. Every chip contains one or two positionable arrays, depending on the width of the array.

Figure 2 shows the layout of a typical positionable WGA, indicating the design parameters that define a particular configuration. An even number of actuator beams is located on every side of the waveguide beams. For one set of actuator beams, the poly-Si is designed in a meandering shape, i.e. all actuator beams on one side are electrically connected in series, creating a two-terminal element.

Positioning requirements can be specified based on the residual misalignment resulting from the assembly. In the final assembly configuration, the chips are mounted through flip-chip technology exploiting small bumps, providing an expected vertical precision of $\pm 1\mu$m per bump. As a result, the expected maximum vertical misalignment from chip to chip is roughly 2μm. Taking into account some margin, we target for 4μm vertical motion range of the WGA.

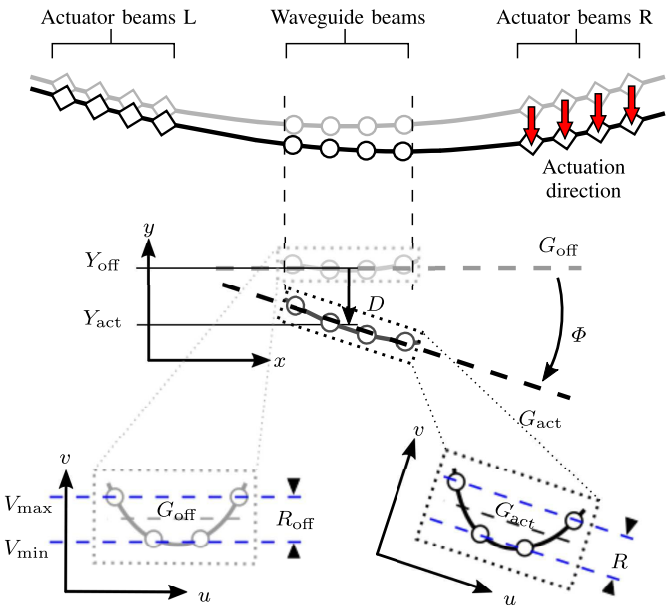

Fig. 3. Schematic representation of a WGA's crossbar shape with one activated actuator side. The positioning of the crossbar is quantified using three positioning indicators: deflection D, angle Φ, and waveguide core range R.

Additionally, the actuators must be able to compensate a rotational misalignment of up to approximately 0.05°, based on a 4μm vertical height difference over a chip size of 5 mm. Furthermore, as the positionable WGAs are designed for alignment to a counter PIC of which the waveguides are located in a flat plane, the WGA's waveguide core positions should not deviate more than 100 nm from a straight line to keep the loss level of all channels acceptable.

The positioning performance is quantified by the introduction of positioning indicators, which are all based on the linear approximation of the positions of the waveguide cores, G, as shown in Figure 3. Initially, so without any actuation, the vertical deflection of the crossbar is represented by Y_{off}, which is measured between the points in the center of the segments where the waveguides are located. Due to the curved shape of the crossbar, the waveguide cores have a certain vertical deflection, V, measured perpendicular to G_{off}. The range of the waveguide cores, R, is defined as the maximum distance between the cores above and below G, or $V_{max} - V_{min}$. In the specific situation without actuation, we refer to this range as R_{off}.

In actuation mode, additional positioning indicators are required to describe the performance of the system. The vertical deflection of the crossbar is now represented by Y_{act}. The range, R, is now measured perpendicular to G_{act}. For this reason, a moving coordinate system (u, v) is introduced, and similar to the intitial situation we define $R = V_{max} - V_{min}$. Positioning parameter D represents the change in vertical deflection with respect to the non-actuated situation, or $Y_{off} - Y_{act}$. Angle Φ is the angle between G_{off} and G_{act}.

III. Modeling

A 3D finite element model is developed in order to comprehend the relation between the WGA design parameters and the positioning indicators. The model takes into account the residual thermal stress from the fabrication process, based on the deposition temperatures of the different materials. This way, the model produces the post-release deformation of the WGA at room temperature. Without actuation, the actuator beams push the outer parts of the crossbar upward while the waveguide beams pull the center of the crossbar downward. The actuator operation of the WGA is also implemented in the model, by imposing a uniform temperature on the actuator beams. When activated, the actuator beams move the crossbar downwards. At the same time, this will also reduce the curvature of the crossbar.

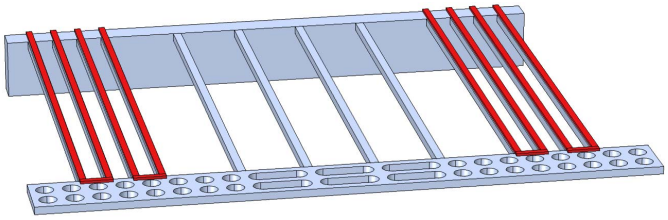

Fig. 4. Representation of the finite element model of the benchmark WGA. This design has four actuator beams (with poly-Si in red) on each side and four waveguide beams in the middle. The WGA includes etch holes in the crossbar, similar to the fabricated WGAs.

Since we are interested in discovering trends rather than developing a very detailed model, the model is kept as simple as possible, which helps to reduce the calculation time. For example, the model does not include the layer of SiO_2 that is deposited on top of the poly-Si in order to protect it from being etched (see [12] for more details on this). Furthermore, the beams in the model have a rectangular cross-section, while they are trapezoidal-shaped in the fabricated devices.

In order to distinguish the effect individual design parameters have on the deformation of the WGA, a benchmark WGA is defined. By varying only one of the design parameters of this benchmark at a time, its isolated influence on the deformation can be determined. The benchmark WGA consists of four waveguide beams and two sets of four actuator beams with a beam length of 800μm, a waveguide beam pitch of 127μm, an actuator beam pitch of 50μm, a poly-Si thickness of 5μm and a crossbar width of 118μm. Figure 4 includes a graphical representation of the finite element model of the benchmark WGA.

The full results of the extensive analysis of all six design parameters are included in the Appendix. In Table I, a qualitative representation of the effect of the different design parameters on the performance of the WGA is provided.

The symbols in the table (which are based on the data in Table IV within the Appendix) indicate how positioning indicators are affected by design parameters. Individual design parameters are increased, causing the positioning indicatorsto either increase (+ and ++), decrease (- and –), or remain unaltered (0). Two symbols indicate a stronger response compared to a single symbol. It must be noted that only column-wise comparison of the symbols is valid. The most dominant design parameters are the beam length, the poly-Si thickness, and the waveguide beam pitch. The influence of the crossbar width, the number of waveguide beams, and

TABLE I

QUALITATIVE EFFECT OF INDIVIDUAL DESIGN PARAMETERS ON WGA PERFORMANCE. THE SYMBOLS INDICATE THE CORRELATIONS WITH RESPECT TO DESIGN PARAMETERS CHANGES. INCREASING A DESIGN PARAMETER LEADS TO A STRONG INCREASE (++), MODERATE INCREASE (+), MODERATE DECREASE (-), STRONG DECREASE (–) OR NO CHANGE OF POSITIONING INDICATORS

Design parameter	Initial deformation		Deformation by actuation		
	ΔY_{off}	ΔR_{off}	ΔD	ΔR	$\Delta \Phi$
Beam length	++	--	++	--	++
Poly-Si thickness ($< 7\,\mu$m)	++	++	++	++	++
Waveguide pitch	-	++	-	++	+
Crossbar width	+	-	+	-	-
Number of wg beams	--	++	--	0	--
Number of actuator beams	+	--	+	0	++

the number of actuator beams was also investigated, but for these design parameters the model outcome indicated a non-significant effect on the WGA performance. According to the model, with increased beam length the crossbar will have a higher initial out-of-plane deflection (Y_{off}), and the waveguide cores will be confined to a smaller range (R_{off}). Also, with larger beam length the motion ranges will increase (D and Φ). The range upon actuation R will reduce less when beam length is increased, i.e. the curvature the crossbar initially has will be reduced upon actuation, but the magnitude of this effect reduces as the beam length increases. Additionally, the model predicts that increasing the poly-Si thickness ($<7\mu$m) leads to a significant increase of all positioning indicators. Finally, the waveguide beam pitch significantly affects the out-of-plane bending stiffness of the crossbar. Hence, with increasing pitch it can be expected that the initial waveguide core range R_{off} increases, which is confirmed by the model. Also, the model indicates that there is a positive correlation between R and the waveguide beam pitch. The model suggests that the positioning performance can be optimized by tuning these design parameters; however, there are trade-offs to be taken into account. For instance, a small Y_{off} in combination with a large D is a conflicting demand, as these cannot be optimized in one design. A very important demand is the high precision in waveguide alignment, which suggests to minimize the values for R_{off}. The model indicates that this can be achieved particularly by reducing the waveguide pitch, and by reducing the poly-Si thickness as well as increasing the beam length.

IV. RESULTS I, EFFECT OF DESIGN PARAMETERS

Figure 5 shows a realized photonic MEMS chip that is singulated, mounted on a custom PCB, and electrically connected to the PCB by wirebonds. Ten waveguide cores are visible, only the middle four of which are used by this specific WGA.

A. Method

The performance of selected realized WGAs is determined by operating the actuators with a *Keithley 2611 system sourcemeter*, while simultaneously measuring the surface contour of the WGA using a *Bruker Contour GT-K 3D* optical

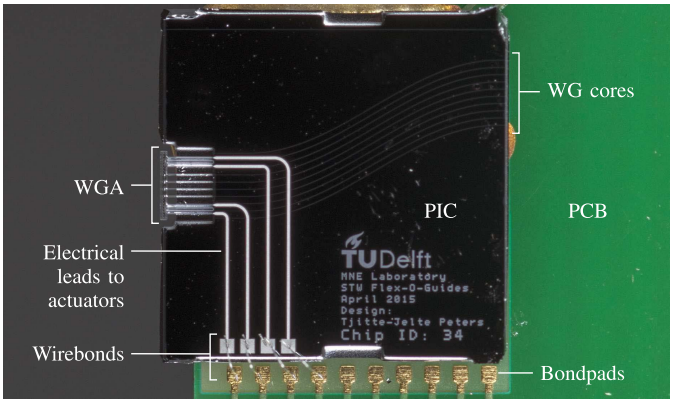

Fig. 5. Photograph (topview) of a realized PIC with positionable waveguide array (type A), mounted on a PCB and electrically connected by wirebonds.

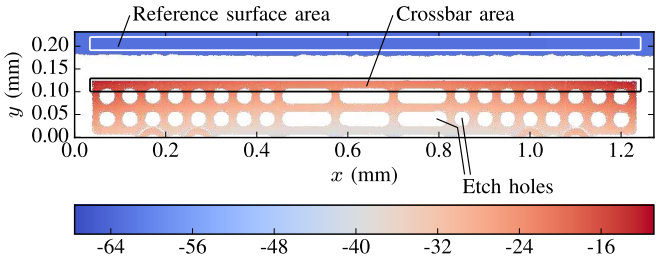

Fig. 6. Surface contour measurement (top view) of a WGA, with the height data in μm. The crossbar area (within the black rectangle) is calibrated by subtracting the reference surface area (within the white rectangle). Extracting a mean profile over the length of the calibrated crossbar area provides the calibrated crossbar profile.

(white light) profilometer. Simultaneous measurement of the crossbar top-surface and a nearby positioned reference surface are performed for different levels of dissipated power in the actuators. The reference surface is used to calibrate the sequential crossbar measurements by providing a common height reference. Figure 6 shows an example of a surface measurement, in which black and white rectangles indicate the regions of the crossbar and reference surface that are used for further analysis. Only the crossbar areas of the WGAs is measured, in order to keep the runtime of the measurement at an acceptable level. A consequence of measuring crossbars (as opposed to measuring the full WGA including the beams) is that only the relative deflection is known, and not e.g. the initial vertical deflection of the crossbar.

Figure 7 shows three exemplifying calibrated crossbar profiles. The presented profiles are obtained from three different measurements: without actuation, actuation of the right side only, and actuation of the left side only. The profiles illustrate the crossbar moves downward upon actuation. Moreover, the noise level of the profiles is higher than the expected surface roughness. The standard deviation of the noise of the calibrated profiles is calculated to be $0.2\,\mu$m. Among the sources of noise are the spikes that occur at a regular pitch, which are a result of the Si_3N_4 cores affecting the measurements of the optical profilometer.

The measured WGAs are operated using three actuation modes, which are defined as follows. **Right:** Operating the

TABLE II
THE MEASURED POWER SENSITIVITIES OF THE TESTED WGAS

ID	T_{Poly} (μm)	W_{Poly} (μm)	WG pitch (μm)	Beam length (μm)	Beam config: wg,act (#)	W_{CB} (μm)	Power sensitivity of D (μm/W) Left	Right	L+R	PS of Φ (°/W) Left	Right	R_{off} (μm)	PS of R (μm/W) L+R
A	3	12	127	800	4,8	118	86	86	174	3.1	-3.3	0.83	-1.1
B	5	12	127	800	4,8	118	103	100	203	5.3	-5.2	1.02	-2.1
C	3	10	50	800	4,8	68	62	67	140	1.1	-2.5	0.17	-0.9
D	3	12	50	1000	4,12	118	86	86	216	1.9	-2.9	0.13	-0.8
E	5	12	250	800	6,12	68	55	61	128	4.5	-4.3	6.32	-21.9
F	5	12	250	1400	4,12	68	175	168	400	8.7	-7.4	2.63	-5.3

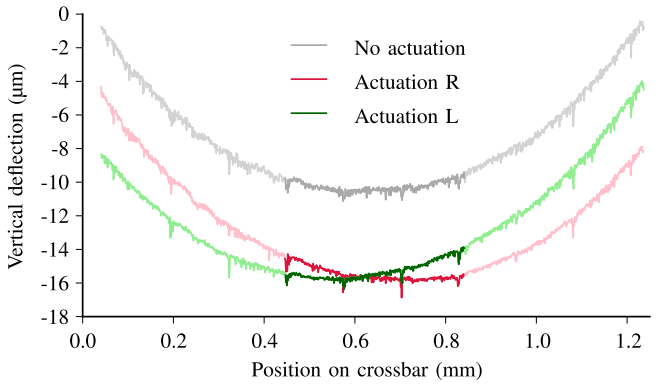

Fig. 7. Three exemplifying calibrated profiles extracted from three surface contour measurements. The darker areas indicate the regions within the two outer waveguide beams.

actuator beams on the right side of the waveguide beams. **Left:** Operating the actuator beams on the left side of the waveguide beams. **R+L:** Simultaneously operating the actuators on both sides of the waveguide beams. The positioning indicators D, Φ, and R are determined using these three actuation modes, so that they can be plotted as a function of dissipated power.

B. Effect of Design Parameters

From the finite element analysis we have an estimation of how the design parameters influence the positioning indicators. Measurements of a benchmark WGA (see Section III for specifications) and a WGA that only differs in actuator layer thickness are used to verify the predicted effect of the poly-Si thickness on the deformation. These two WGAs will be referred to as WGA A (3μm thick poly-Si) and WGA B (5μm thick poly-Si).

The model outcome of WGA A and WGA B is presented in Figure 8. The vertical deflection D, crossbar angle Φ, and vertical range of the waveguide core positions R are plotted as a function of actuator temperature. The measurement results of WGA A and WGA B are presented in Figure 9, showing the vertical deflection D, crossbar angle Φ, and vertical range of the waveguide core positions R as a function of power dissipated in the actuator(s). A positive D corresponds to a downward movement of the crossbar. In previous work it is estimated that 60 mW of dissipated power corresponds to an actuator temperature of 240°C [12].

D and Φ are zero in the non-actuated state. Since the crossbar does have an initial curvature, the value for R_{off} is not zero. Both the model and measurement results show that WGA B has increased values for D and Φ as compared to WGA A. Furthermore, the R values of WGA B are higher than those of WGA A, in the model as well as in the measurements. These observations are also in agreement with the data in Table I, where an increase in poly-Si thickness corresponds to an increase of all the positioning indicators.

One aspect where the model and measurement differ is the magnitude of the values on the vertical axes. This difference is a direct result of the model differing from the actual WGA. As explained above, the protecting layer of SiO_2 is not incorporated in the model. Absence of this layer will lead to deviations, the extent of which varies per positioning indicator. For example, the measured D and Φ being slightly smaller than the modeled D and Φ can be explained by the extra stiffness that follows from the thin layer of SiO_2. The R on the other hand, is larger in the measurements than in the model results. This is explained by the residual compressive stress in the SiO_2 layer, increasing the curvature of the crossbar.

Table II summarizes the measured positioning performance of the WGAs. A relevant measure for comparison is the power sensitivity (PS) of the positioning indicators. The PS is essentially the slope of the data shown in Figures 8 and 9.

The modeling suggested dependencies of positioning performance on other design parameters as well. Four additional WGAs, C through F, were available to experimentally verify these dependencies. The measured positioning performance results of these WGAs are available as supplemental material, and their measured positioning performance is included in Table II.

An optimal design has maximum PS for D and Φ, whereas the initial postrelease range R_{off} is minimal. WGAs C through F provide indications how design parameters can be used for optimization. It must be noted that in these WGA designs sometimes multiple design parameters are changed, hence comparison must be done with some care. However, a few observations can clearly be made.

1) Maximize PS of D: The modeling results indicated that maximum PS for D is particularly achieved with longer beams. The effect of waveguide beam pitch is not significant. This is supported by the measurements. WGA C and D have smaller pitch compared to WGA A, while they have the same poly-Si thickness. The values for D are in a similar range, however.

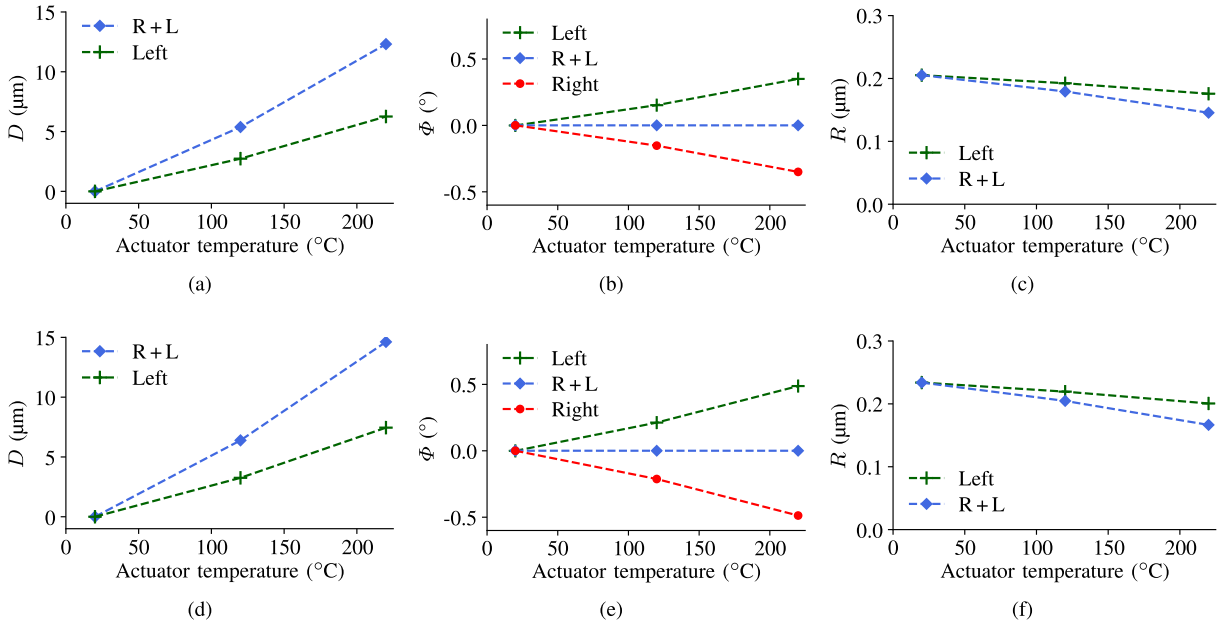

Fig. 8. The modeled positioning performance of WGA A (3μm poly-Si thickness, (a), (b) and (c)) and WGA B (5μm poly-Si thickness, (d), (e) and (f)).

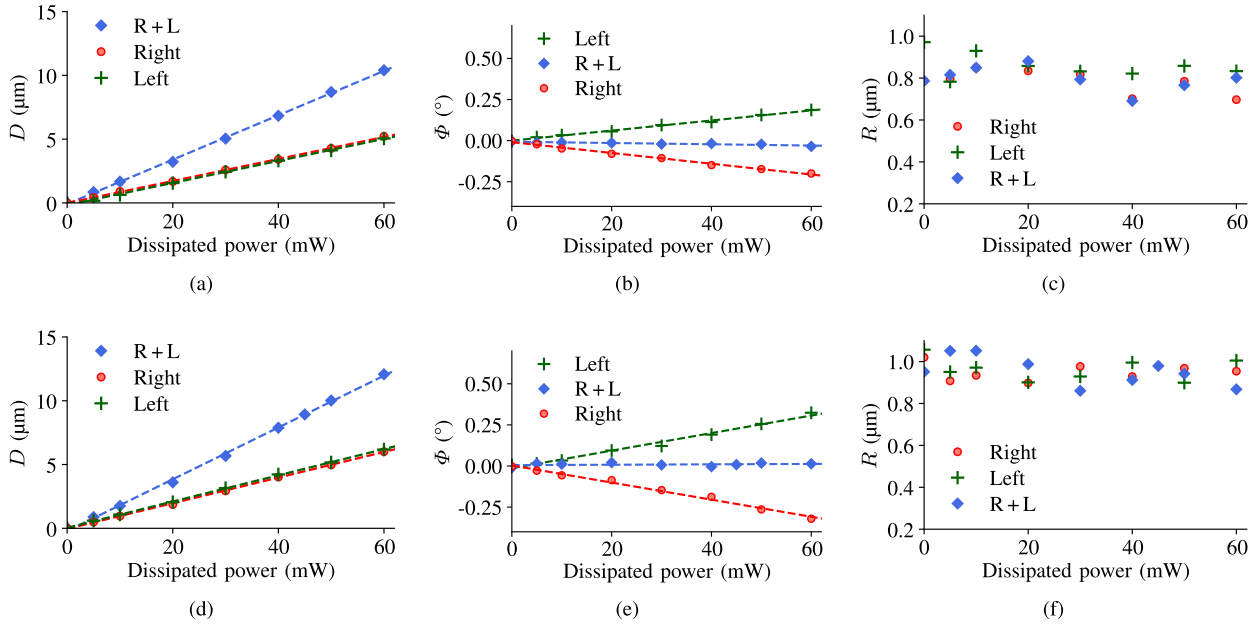

Fig. 9. The measured positioning performance of WGA A (3μm poly-Si thickness, (a), (b) and (c)) and WGA B (5μm poly-Si thickness, (d), (e) and (f)).

WGA F, on the other hand, has very long beams, and the measurements clearly indicate that this is dominant for the PS of D, even though the waveguide pitch is much larger (which has a small negative effect on PS of D).

2) Maximize PS of Φ: The maximum PS for Φ is mostly driven by beam length and poly-Si thickness, according to the modeling results. In the measurements, the smallest PS of Φ is observed for WGA C, which is indeed the design with the shortest beams and the thinnest layer of poly-Si. The largest values for the PS of Φ are measured with WGA F. As suggested by the model, this particular WGA has the longest beams and thickest poly-Si layer of the devices that were measured.

3) Minimize Postrelease R_{off}: Apart from the poly-Si thickness, it is particularly the waveguide pitch and number of waveguide beams that is dominating the waveguide range R_{off}. It must be observed in Table II that the PS for R is in μm/W. This means that with operation powers of $\sim$ 100 mW the value for R is affected by roughly 0.1μm (WGA A, C, D) or 0.2μm (WGA B). This indicates that a well-performing design needs to have values for R_{off} (i.e. only determined by the initial postrelease deformation) in the order of or less than 0.1μm to 0.3μm. Table II shows that WGA C and D have by far the best performance for R_{off}. These are indeed the designs with the smallest waveguide pitch (50μm) and the smallest poly-Si thickness. Moreover, WGA D, which is 200μm longer

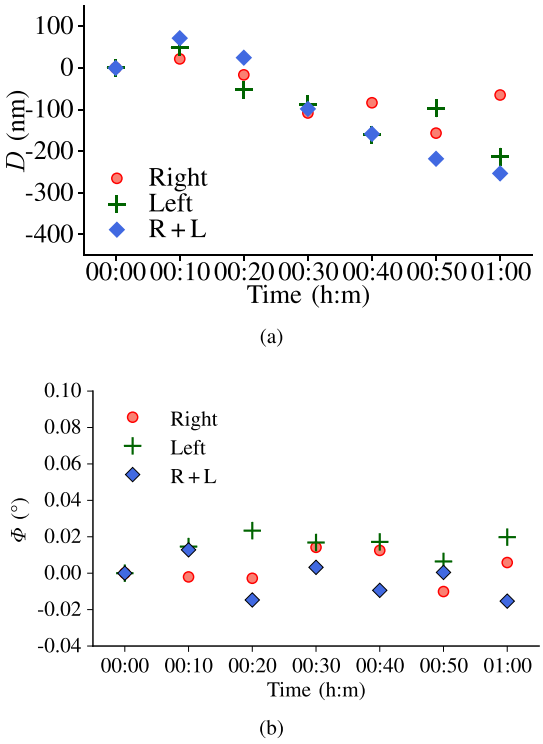

Fig. 10. The deflection D and angle Φ of WGA D in the three operation modes, measured over a total duration of one hour.

than WGA C, has a smaller R_{off}, which corresponds with the model outcome.

V. Results II, Photonic Alignment Experiments

This Section investigates two more aspects that are relevant to the operation of the WGAs in an active alignment scheme: actuator stability, and mode fields of etched facets. Finally, optical coupling of a positionable WGA with a counter PIC is demonstrated and measured.

A. Actuator Stability

The stability of WGA D is studied by operating the actuators with the system sourcemeter at a constant voltage, while performing a surface contour measurement with the white light profilometer every ten minutes, for a total duration of one hour. A single measurement takes approximately five seconds. The obtained Y and Φ results provide a figure of merit for the stability of the actuators over time.

WGA D is subjected to stability measurements which are performed at the three different operation modes, using 50 mW of dissipated power. Figure 10(a) includes the measured Y as a function of time. The vertical deflection of every actuator mode's first measurement (time=00:00) is aligned with the zero point of the vertical axis. All three actuation modes show the same trend: Y first increases a little bit, and then decreases. The measurements reveal a maximum change in deflection of 92 nm, 64 nm, and 71 nm for the Right, Left, and R+L actuation respectively.

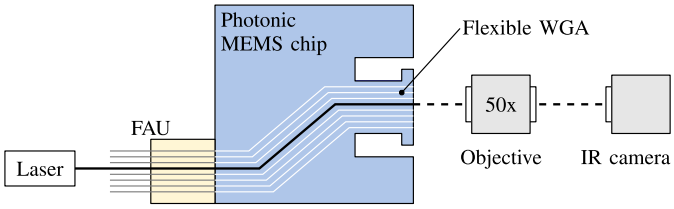

Fig. 11. Schematic representation of the experimental setup used for the mode field analysis. The laser source is operated at 1550 nm.

The measured Φ as a function of time is presented in Figure 10(b). The angle Φ of every actuator mode's first measurement (time=00:00) is aligned with the zero point of the vertical axis. The measurements reveal a maximum change in Φ of 0.023°, 0.011° and 0.028°, for the Right, Left, and R+L operation mode respectively.

A precise alignment requires stability in the position of the crossbar until it is mechanically fixed. For most fixing methods, the fixation will be accomplished in a matter of seconds, resulting in far less than 10 nm deviation from the aligned optimum. Regardless of the fixing method, an active alignment approach enables small adjustments of the actuators until the fixation is finished in order to maintain an optimal optical alignment. The stability of the positionable WGAs is acceptable.

B. Mode Field Analysis

The fabricated waveguides differ from conventional Si_3N_4/SiO_2 waveguides on two fronts. Firstly, material alongside and underneath the waveguide beams is removed, resulting in suspended waveguide beams. Secondly, the end-facets are etched, leading to a topography on the facet. This Subsection measures the mode field profiles of the fabricated suspended waveguides to have a first verification of their quality.

The mode field intensity distribution of the waveguides is studied by coupling light into the waveguides of a photonic MEMS chip through a fibre array unit (FAU). The photonic MEMS chip is first mounted to a PCB, after which the FAU is mounted to it with a UV-curable epoxy. A photonic MEMS chip with eight channels (900μm beam length and 127μm waveguide pitch) is selected in combination with an eight-channel FAU (with similar 127μm waveguide pitch). The waveguide cores measure 1μm $\times$ 220 nm (width $\times$ thickness).

Using a *Keysight 8163B* tunable laser and a *Xenics Xeva XC-132* infrared (IR) camera, near field profiles of all the photonic channels are obtained consecutively. The schematic of the experimental setup is presented in Figure 11. The tunable laser, operating at 1550 nm, is connected to one of the channels, while the IR camera and a 50$\times$ objective (*Olympus 1-LM550*) are used to capture the mode field intensity distribution at the end facet of the suspended waveguide corresponding to the active channel.

Figure 12 includes the measured mode field profile of the first waveguide channel. The measured mode field profiles of the remaining waveguide channels are available as supplemental material. With a specified focal length of 3.6 mm and a measured distance between objective and camera

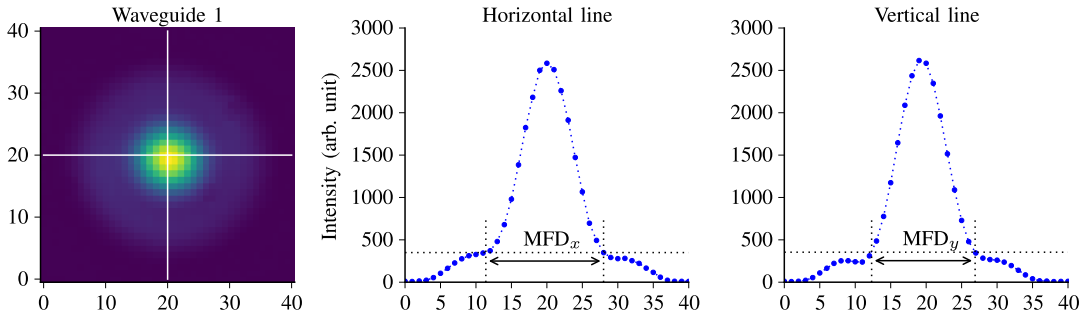

Fig. 12. The measured mode field intensity distribution of waveguide 1. The 2D image as measured with the IR camera is shown on the left, with the values at both axes corresponding to camera pixels. The profiles along the horizontal and vertical white lines are shown in the two graphs on the right, with the Gaussian $1/e^2$ mode field diameters indicated.

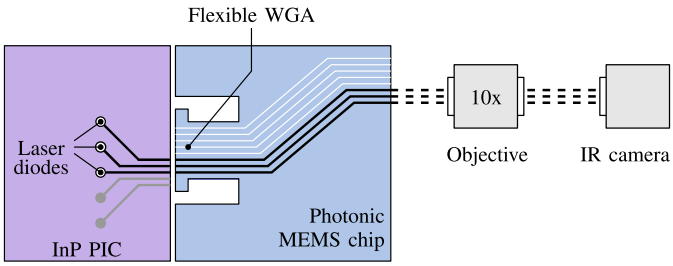

Fig. 13. Schematic representation of the experimental setup used for the photonic alignment experiment.

TABLE III
THE MATERIAL PROPERTIES AS USED IN THE FINITE ELEMENT MODEL

Material	Coefficient of thermal expansion (1/K)	Young's modulus (GPa)	Poisson's ratio	Density (kg/m^3)
SiO_2	0.5×10^{-6}	70	0.17	2200
Poly-Si	$\alpha_{Si}(T)$	160	0.22	2320

of 61 cm, the magnification of the optical system is calculated to be approximately 168 times, resulting in one camera pixel (measuring 30μm by 30μm) corresponding to 178 nm by 178 nm. Based on Figure 12, the Gaussian $1/e^2$ mode field diameters can be estimated. Waveguide 1 is measured to have a horizontal mode field diameter (MFD$_x$) of about 2.9μm and a vertical MFD$_y$ of 2.6μm. For all eight channels, mean values for MFD$_x$ and MFD$_y$ of (2.81 $\pm$ 0.06) μm and (2.63 $\pm$ 0.06) μm were measured, respectively. The measured mode field profiles do not show any abnormalities and demonstrate that the partly suspended waveguide beams function properly.

C. Photonic Alignment Experiment

Finally, the suitability of a positionable WGA for photonic alignment is evaluated by means of a photonic alignment experiment. For this experiment, a waveguide pitch of 50μm was selected, as this is the only configuration that allows for simultaneously aligning more than two waveguides. Figure 13 presents the schematic of the experimental setup, consisting of a photonic MEMS chip, an indium phosphide (InP) PIC, a 10$\times$ objective, and an IR camera.

For monitoring the coupled power, the 10$\times$ objective and the IR camera are used, providing an image of the end-facets on the opposite side of the photonic MEMS chip. Using this configuration, the IR camera can capture three adjacent 50μm-pitched waveguide spots simultaneously in a single frame. First, for pre-alignment, the laser sources (operating at a wavelength of 1550 nm) on the InP PIC are activated, and the actuators on the photonic MEMS chip are temporarily set to approximately 50 % of their maximum range. Then, using manual microstages, the InP PIC is aligned with respect to the WGA side of the photonic MEMS chip, aiming for maximum light coupling through the waveguides that are in the field of view.

Traversing the complete actuator range in a scan-like fashion from 0 V to 55 V in steps of 1 V provides a total of 3136 frames, each one representing the mode field intensity distribution of the three waveguides within the field of view of the camera. From every frame, the intensity amplitude of the three spots is extracted using a two-dimensional gaussian fit. Figure 14 presents the resulting normalized intensity scans for the three waveguide spots.

For all three spots, no light was measured at a voltage of 0 V across both actuators. At this voltage, the waveguide cores at the free end of the flexible WGA are located above the InP waveguide cores. Similarly, also at an actuator voltage of 55 V, no light was measured at the three spots. This corresponds to the situation in which the positionable waveguide cores are located below the InP waveguide cores. At intermediate actuator voltages, alignment of the positionable waveguide cores with the InP waveguide cores is achieved, where the maximum intensity amplitude indicates an optimal alignment (see Figure 14).

By combining the individual intensity scans, a representation of the overall alignment is obtained, which is presented in Figure 15. The combined colormap is obtained by multiplying the normalized intensities of the three waveguide spots. The best alignment of all three waveguides within the traversed actuator range occurs at a voltage of 42 V and 2 V, for the left and right actuator respectively.

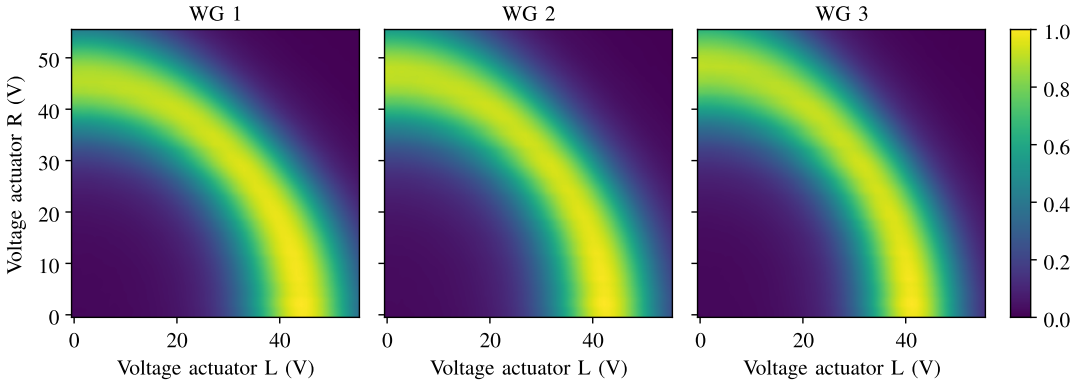

Fig. 14. Colormap of the normalized intensity amplitude as a function of left and right actuator voltage, measured at the three waveguides.

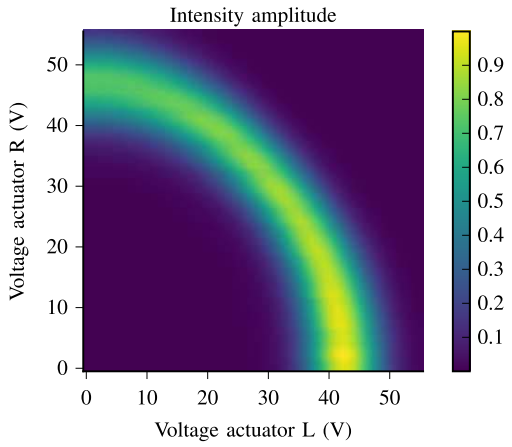

Fig. 15. The normalized amplitude of the combined measured intensity as a function of actuator voltage.

VI. Final Discussion and Conclusions

Positionable photonic waveguide arrays were developed for a novel chip-to-chip alignment concept. A finite element model of the positionable waveguide arrays was created in order to understand how the design influences the performance of the WGA. This investigation provides insights that are not only relevant to the WGAs as applied in the proposed alignment concept, but are also valuable for the development of similar systems. The model outcome is validated by means of measurements performed on fabricated WGAs.

The main design parameters that affect the performance are the poly-Si thickness, the beam length and the waveguide pitch. The power sensitivities of D, R, and Φ particularly increase with longer beams and thicker poly-Si. R_{off} improves with longer beams, smaller waveguide beam pitch and thinner poly-Si. It is apparent that for example the requirements for a small R_{off} and a large PS of D conflict with respect to the poly-Si thickness. However, the modeling results provide guidelines for the design parameters, directing towards an optimal positionable WGA design.

For a WGA to have a large PS of D, a large PS of Φ, and a small R_{off}, a feasible design has a poly-Si thickness of 3μm, a waveguide pitch of 50μm, and a beam length of 1000μm. Measurements revealed that a WGA with this design meets the requirements by achieving an out-of-plane deflection D and rotation Φ that are sufficiently large while the initial waveguide core range R_{off} is small enough. At the same time, this WGA design results in a relatively large initial deflection Y_{off}, which makes planar photonic alignment with another PIC difficult. This issue can be solved by a smart design of the total system, which is part of ongoing research in our lab.

Drifts of 10 nm min^{-1} and 0.003° min^{-1} were determined for deflection and angle, based on measurements spanning one hour in total. Moreover, mode field analysis of an eight-channel WGA confirms that the partly suspended Si_3N_4/SiO_2 waveguides provide proper photonic functionality. An average MFD of $2.63\mu\text{m} \times 2.81\mu\text{m}$ was measured for suspended waveguide beams having 220 nm $\times$ 1μm sized waveguide cores. Finally, it was shown that a working WGA can be designed which can accomplish submicrometer photonic alignment. To this end, three adjacent channels of a selected WGA were actively aligned with three channels of another PIC.

Appendix

A finite element model is developed to understand the effect of design parameters on the deformation and the positioning indicators of the WGA. A benchmark system is defined with the following design parameters: four waveguide beams and eight actuator beams with a beam length of 800μm, waveguide pitch of 127μm, poly-Si thickness of 5μm and a crossbar width of 118μm. By varying only one of the design parameters at a time, the expected influence of that specific parameter on the positioning indicators is determined.

In order to keep the calculation times to a minimum, the model is simplified as much as possible. The most important approximations of the model are discussed here. The waveguide beams are approximated by SiO_2 beams, and the Si_3N_4 waveguide cores are not included. Furthermore, all the beams in the model have a rectangular cross-section, while the fabricated devices have slightly slanted sidewalls (due to the etching process). Additionally, the model does not include the layer of SiO_2 that is deposited on top of the poly-Si in order to protect it from being etched (see [12] for more details on this). For the thermal actuators, a uniform temperature is applied to the poly-Si strips and the supporting

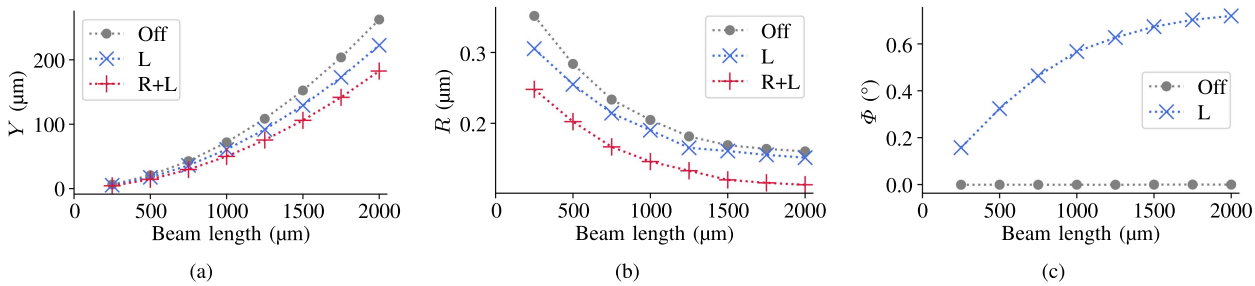

Fig. 16. The modeled (a) postrelease deflection Y, (b) range R, and (c) angle Φ as a function of the beam length.

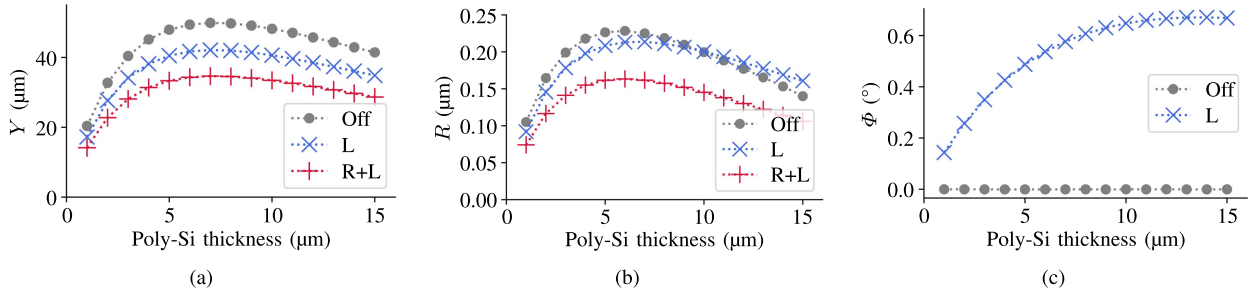

Fig. 17. The modeled (a) postrelease deflection Y, (b) range R, and (c) angle Φ as a function of the poly-Si thickness.

SiO_2 beams, rather than implementing Joule heating. The crossbar is provided with etch holes similar to the ones in the fabricated devices, in order to accurately emulate the stiffness of the crossbar.

The material properties that are used in the model are presented in Table III. The coefficient of thermal of expansion of poly-Si is implemented as a function of temperature, based on the empirical formula by Okada and Tokumaru [13]:

$$\alpha_{\mathrm{Si}}(T) = c_1\left(1 - e^{-c_2(T-c_3)}\right) + c_4 T, \tag{1}$$

with

$$\begin{aligned} c_1 &= 3.725 \times 10^{-6}, \\ c_2 &= 5.88 \times 10^{-3}, \\ c_3 &= 124, \\ c_4 &= 5.548 \times 10^{-10}. \end{aligned}$$

The predicted effect of the beam length on Y, R, and Φ is presented in Figures 16(a) to 16(c), respectively. The postrelease deformation (the state at room temperature without actuation) is indicated by the grey curve (labeled 'Off' and with filled circles as marker symbol).

Two actuated situations are included in the graphs, the blue curve (labeled 'L' and with crosses as marker symbol) representing actuation of the left side and the red curve (labeled 'R+L' and with plusses as marker symbol) representing simultaneous actuation of both sides. For the actuated state, an actuator temperature of 220 °C is applied.

The plots in Figure 16 show that the various positioning indicators have clear trends as a function of beam length. In order to quantify these trends, values are extracted from the plots indicating the effect on the initial situation and on the situation with actuation. For the initial deformation, the curves labeled 'Off' are relevant. From Figure 16(a) we see that the initial deflection Y_{off} changes from almost zero (at the shortest beams) to more than 250μm (at the longest beams), amounting to $\Delta Y_{\mathrm{off}} = Y_{\mathrm{off}}^{\max} - Y_{\mathrm{off}}^{\min} =$ an increase of 256μm. Similarly, Figure 16(b) provides (based on the grey curve labeled 'Off') $\Delta R_{\mathrm{off}} = R_{\mathrm{off}}^{\min} - R_{\mathrm{off}}^{\max} =$ a decrease of 191 nm.

For the effect of actuation, the difference between the initial ('Off') and actuated ('R+L or L') curves is analyzed. Looking at Figure 16(a) again, we see that the difference between the initial deflection ('Off') and the deflection due to simultaneous actuation ('R+L') changes from almost zero (at the shortest beams) to 78μm (at the longest beams). In other words: $\Delta \mathrm{D} = D_{\max} - D_{\min} = (Y_{\mathrm{off}}^{\max} - Y_{\mathrm{R+L}}^{\max}) - (Y_{\mathrm{off}}^{\min} - Y_{\mathrm{R+L}}^{\min}) =$ 78μm$-$0μm amounting to an increase of 78μm. The change of the range R as a function of beam length is extracted from Figure 16(b) by also looking at the minimum and maximum difference between the initial range ('Off') and the range at simultaneous actuation ('R+L'). The range R decreases more with short beams as it does with longer beams: $\Delta R = (R_{\mathrm{off}}^{\min} - R_{\mathrm{R+L}}^{\min}) - (R_{\mathrm{off}}^{\max} - R_{\mathrm{R+L}}^{\max}) =$ a decrease of 57 nm. Finally, a value for the change in angle Φ is obtained from Figure 16(c). At the shortest beam length, actuation of the left side rotates the crossbar by almost 0.2°, while a rotation of more than 0.6° is achieved with the longest beams. Hence, the actuated angle Φ increases by 0.56° over the modeled beam length range, or $\Delta\Phi = (\Phi_{\mathrm{off}}^{\max} - \Phi_{\mathrm{L}}^{\max}) - (\Phi_{\mathrm{off}}^{\min} - \Phi_{\mathrm{L}}^{\min}) = 0.56°$.

Additionally, the trends of Y, R, and Φ as a function of the poly-Si thickness, the waveguide pitch, the crossbar width, the number of waveguide beams, and the number of actuator beams are presented in Figures 17 to 21. Values representing the trends are acquired in a similar way as it was done for the beam length.

Table IV includes the acquired values, providing a quantitative representation of the effect of the different design parameters on the positioning indicators. Every row represents

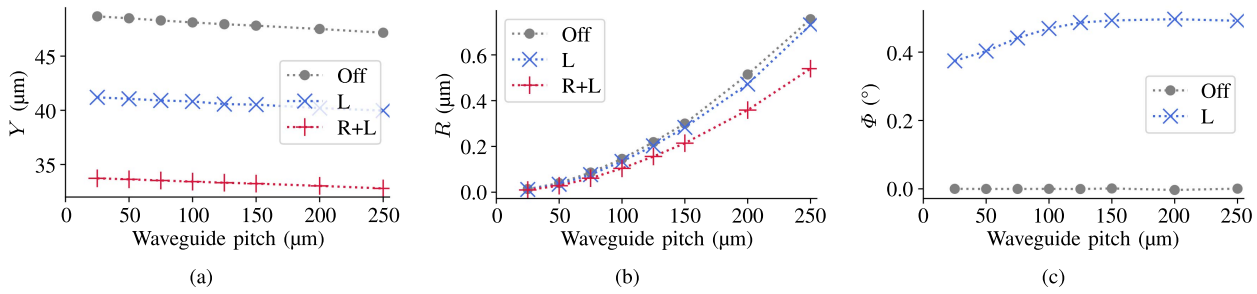

Fig. 18. The modeled (a) postrelease deflection Y, (b) range R, and (c) angle Φ as a function of the waveguide beam pitch.

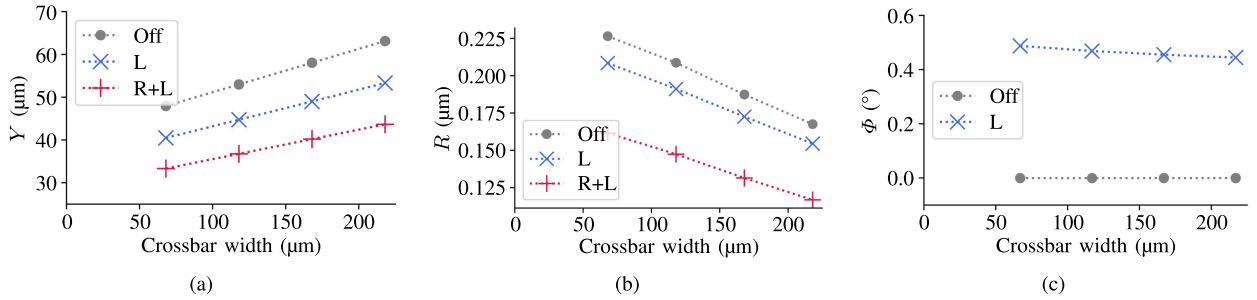

Fig. 19. The modeled (a) postrelease deflection Y, (b) range R, and (c) angle Φ as a function of the crossbar width.

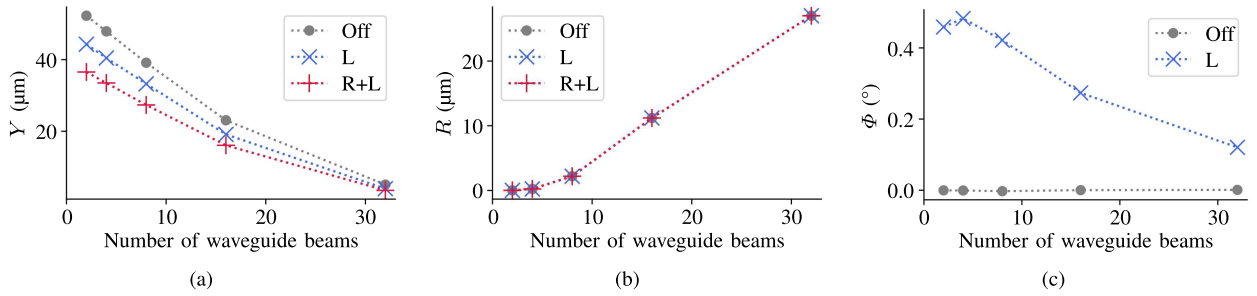

Fig. 20. The modeled (a) postrelease deflection Y, (b) range R, and (c) angle Φ as a function of the number of waveguide beams.

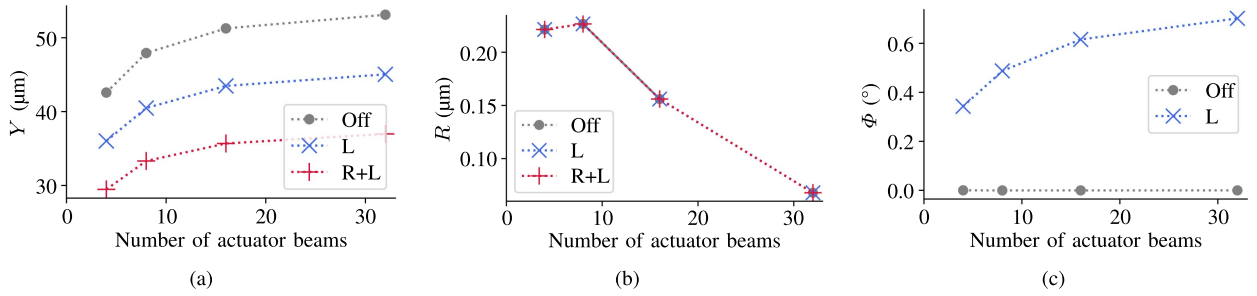

Fig. 21. The modeled (a) postrelease deflection Y, (b) range R, and (c) angle Φ as a function of the number of actuator beams.

a design parameter that is increased over the specified range, whereas the columns display the corresponding change in positioning indicators. The poly-Si thickness is split into two regions, because of the peak in D and R around 7μm. The values in Table IV can be used to compare the influence of different design parameters on a single positioning indicator. In order to accentuate the most dominant relations, a threshold value is introduced, specified as half the average of the absolute values in the same column. Only the values that exceed this threshold value are regarded as significant (++ or --) relations.

In Table IV, the most dominant correlations are indicated by shaded cells. A correlation is considered to be dominant if a cell's absolute value is larger than half of the average of all the absolute values of the corresponding column. For the row representing the number of waveguide beams, the value

TABLE IV

QUANTITATIVE EFFECT OF INDIVIDUAL DESIGN PARAMETERS ON WGA PERFORMANCE. THE VALUES INDICATE THE CORRELATIONS WITH RESPECT TO DESIGN PARAMETER CHANGES. INCREASING A DESIGN PARAMETER LEADS TO A CHANGE OF POSITIONING INDICATORS. THE MOST DOMINANT CORRELATIONS ARE INDICATED BY THE SHADED CELLS

Design parameter	Parameter values	Initial deformation		Deformation by actuation		
		ΔY_{off} (µm)	ΔR_{off} (nm)	ΔD (µm)	ΔR (nm)	$\Delta\Phi$ (°)
Beam length	250 µm to 2000 µm	256.2	−191	78.0	−57	0.56
Poly-Si thickness	1 µm to 7 µm	29.5	123	9.0	34	0.43
Poly-Si thickness	7 µm to 15 µm	−8.5	−85	−2.5	−29	0.09
Waveguide pitch	25 µm to 250 µm	−1.5	742	−0.6	212	0.12
Crossbar width	68 µm to 218 µm	15.2	−59	4.8	−14	−0.04
Number of wg beams	2 to 32 beams	−47.2	26 999	−14.1	0	−0.36
Number of actuator beams	4 to 32 beams	10.5	−159	3.0	0	0.36
Half the average of the absolute values		26.3	113	8.0	25	0.14

corresponding to R_{off} is neglected in calculating the average value, as this value has an extreme deviation from the average. According to the shaded cells, the most significant design parameters are the beam length, the poly-Si thickness, the waveguide beam pitch, the number of waveguide beams, and the number of actuator beams. However, as for functional systems the number of actuator beams usually scales with the number of waveguide beams, the effects of individually increasing waveguide beams and actuator beams are attenuated, and we do not consider them to be dominant design parameters. Below, the trends of the beam length, the poly-Si thickness, and the waveguide beam pitch are discussed.

Increasing the beam length significantly elevates Y_{off}, D, and Φ, improves R_{off}, but reduces R, according to the model. This is as can be expected. Longer beams have the same beam curvature over a longer distance, amounting to an increased Y_{off} as a function of beam length. When actuated, the curvature decreases, and this effect is amplified with longer beams, leading to Y and Φ increasing as a function of beam length. Moreover, as longer beams are more compliant than shorter beams, the crossbar will be less deformed by the waveguide beams and actuator beams as the beam length increases. This results in R_{off} and R decreasing as a function of beam length.

For the poly-Si thickness, only the trends below a value of 7μm are considered. The model predicts that increasing the poly-Si thickness has a positive and significant effect on all positioning indicators. This is in agreement with the theoretical models (e.g., the Timoshenko composite beam theory) describing the curvature of bilayer beams.

Increasing the waveguide beam pitch has a significant positive effect on R_{off} and R, and a less significant effect on the other positioning indicators, according to the model. As the waveguide beam pitch increases, the length of the crossbar grows. The longer the crossbar, the more compliant it will be. In the un-actuated state, the actuator beams will push the sides of the crossbar upwards, while the waveguide beams tend to pull the center of the crossbar down. Hence, it can be expected that, as the waveguide pitch increases, the crossbar will be more deformed, and R will increase. In the actuated situation, a crossbar that is more compliant and deformed due to a larger waveguide pitch is easier to straighten by actuating both sides simultaneously as compared to a crossbar that is less deformed but stiffer due to a smaller waveguide pitch.

ACKNOWLEDGMENTS

The authors would like to thank Ronald Dekker (XiO Photonics) for mounting the FAU to one of the photonic MEMS chips. Furthermore, they thank Rui Santos (Eindhoven University of Technology) for the help with the photonic alignment experiments and the Photonic Integration group of Eindhoven University of Technology for the InP chip design and fabrication. Additionally, they thank the TU Delft Quantum Technology group, and Arjan Beukman in particular, for the help with wirebonding. The Electronic and Mechanical Support Division of TU Delft (DEMO) is acknowledged for the development of the PCBs.

REFERENCES

[1] R. Nagarajan *et al.*, "Large-scale photonic integrated circuits," *IEEE J. Sel. Topics Quantum Electron.*, vol. 11, no. 1, pp. 50–65, Jan. 2005.

[2] N. Pavarelli, J. S. Lee, and P. A. O'Brien, "Packaging challenges for integrated silicon photonic circuits," *Proc. SPIE*, vol. 9133, pp. 91330F-1–91330F-9, May 2014, doi:10.1117/12.2058559.

[3] F. A. Kish, "The past, present, and future of photonic integrated circuits in optical communications," in *Proc. 73rd Annu. Device Res. Conf. (DRC)*, pp. 23–24, Jun. 2015.

[4] N. Pavarelli *et al.*, "Optical and electronic packaging processes for silicon photonic systems," *J. Lightw. Technol.*, vol. 33, pp. 991–997, Mar. 1, 2015.

[5] T.-J. Peters, M. Tichem, and U. Staufer, "Suspended photonic waveguide arrays for submicrometer alignment," *Proc. SPIE*, vol. 9133, pp. 913317-1–913317-10, May 2014, doi:10.1117/12.2052430.

[6] F. Chollet, "Devices based on co-integrated MEMS actuators and optical waveguide: A review," *Micromachines*, vol. 7, no. 2, p. 18, 2016.

[7] T. Bakke, C. P. Tigges, J. J. Lean, C. T. Sullivan, and O. B. Spahn, "Planar microoptomechanical waveguide switches," *IEEE J. Sel. Topics Quantum Electron.*, vol. 8, no. 1, pp. 64–72, Jan. 2002.

[8] M. W. Pruessner, N. Siwak, K. Amarnath, S. Kanakaraju, W.-H. Chuang, and R. Ghodssi, "End-coupled optical waveguide MEMS devices in the indium phosphide material system," *J. Micromech. Microeng.*, vol. 16, pp. 832–842, Mar. 2006.

[9] Y. W. Kim, M. G. Allen, and N. F. Hartman, "Micromechanically based integrated optic modulators and switches," *Proc. SPIE*, vol. 1793, pp. 183–189, Mar. 1993, doi:10.1117/12.141215.

[10] J. Brière, P.-O. Beaulieu, M. Saidani, F. Nabki, and M. Menard, "Rotational MEMS mirror with latching arm for silicon photonics," *Proc. SPIE*, vol. 9375, p. 937507, Feb. 2015, doi:10.1117/12.2077033.

[11] K. Wörhoff, R. G. Heideman, A. Leinse, and M. Hoekman, "TriPleX: A versatile dielectric photonic platform," *Adv. Opt. Technol.*, vol. 4, no. 2, pp. 189–207, 2015.

[12] T.-J. Peters and M. Tichem, "Electrothermal actuators for SiO_2 photonic MEMS," *Micromachines*, vol. 7, no. 11, p. 200, 2016.

[13] Y. Okada and Y. Tokumaru, "Precise determination of lattice parameter and thermal expansion coefficient of silicon between 300 and 1500 k," *J. Appl. Phys.*, vol. 56, no. 2, pp. 314–320, 1984.

Tjitte-Jelte Peters received the B.Sc. and M.Sc. degrees in electrical engineering from the University of Twente, The Netherlands. During his education, he specialized in microsystems and microelectronics in the Transducers Science and Technology Group. After working at an engineering company for almost a year, he joined the Delft University of Technology in 2012, as a Ph.D. Candidate with the Micro and Nano Engineering Laboratory. His main field of interest is the microfabrication of MEMS.

Marcel Tichem was a Research Fellow in the Optical and Semiconductor Devices Group, Imperial College, London, in 2011, to investigate volume methods for nano-particle patterning. He is currently an Associate Professor with the Department of Precision and Microsystems Engineering, Faculty of Mechanical, Maritime, and Materials Engineering, Delft University of Technology. He also leads a program on micro- and nano-scale assembly. Topics of interest include microfabrication and MEMS for photonic alignment, self-assembly, and nano-scale heterogeneous patterning.